Advances in Science and Technology Research Journal

Advances in Science and Technology Research Journal, 2026, 20(10), 468–480
https://doi.org/10.12913/22998624/231503
ISSN 2299-8624, License CC-BY 4.0

Received: 2026.07.15
Accepted: 2026.08.21
Published: 2026.09.01

Model-based corrosion and operational risk assessment of a representative Caspian Sea subsea pipeline

Nurlan Abdullazade[1]

[1] Doctoral Candidate, Azerbaijan State Oil and Industry University, Baku, Azerbaijan
E-mail: abdullazadanurlan@gmail.com

ABSTRACT

Gas pipelines on the floor of the South Caspian have to cope with a set of loads that seldom occur together anywhere else: an aggressive, CO_2- and H_2S-bearing produced fluid, multiphase flow, a steep temperature drop between the wellhead and the seabed, and a tectonically restless basin dotted with mud volcanoes. This paper asks a focused question — for a representative rather than field-measured 70 km line, how do two standard CO_2-corrosion correlations behave, how sensitive is the answer to the main operating variables, and how does the resulting wall loss propagate into mechanical and operational risk? The de Waard–Milliams (1991) and NORSOK M-506 (2017) models are applied along the route using the correct total-pressure form of the fugacity coefficient and NORSOK's tabulated temperature interpolation, and H_2S is handled where it actually matters — as a sour-service and cracking constraint screened against ISO 15156 / NACE MR0175 rather than as a general-corrosion term.Because the inputs are assumptions, the numbers are illustrative of the framework, not predictions for a specific asset. With that caveat, the two models give inlet corrosion rates of roughly 11–16 mm/yr under the hottest, highest-CO_2 conditions, falling below 1 mm/yr at the cold outlet. The more interesting result is that the models do not simply differ by a fixed margin: NORSOK M-506 is far more aggressive than de Waard–Milliams through the 20–60 °C band — by up to three- to fourfold — but the two cross over near the seabed temperature, where NORSOK's temperature constant collapses and de Waard–Milliams becomes the more conservative of the two. A one-at-a-time sensitivity study ranks CO_2 partial pressure, temperature and total pressure as the dominant levers (factors of ×1.5 to ×2.8 over realistic ranges), and a 10,000-sample Monte Carlo propagates the input ranges into full predictive distributions. Wall thinning is then carried into a Timoshenko–Gere collapse check and a DNV-RP-F101 burst assessment, and the operational hazards are consolidated into a 5×5 risk matrix with explicit likelihood and consequence definitions. Internal CO_2 corrosion emerges as the controlling degradation mechanism, and — given the crossover — the safe design choice is the envelope of the two models rather than either one alone.

Keywords: Caspian Sea; subsea gas pipelines; CO_2 corrosion modelling; de Waard–Milliams; NORSOK M-506; fugacity; model crossover; H_2S sour-service screening; hydrate formation; Monte Carlo; risk-based inspection.

INTRODUCTION

Offshore oil and gas remain central to global energy supply, and the subsea pipelines that move produced hydrocarbons to shore are among the least forgiving assets an operator owns. A line on the seabed cannot be walked, rarely be inspected without specialised tooling, and never be repaired quickly. Its integrity therefore has to be reasoned about in advance, from the chemistry of the fluid it carries and the environment it sits in, long before any defect becomes visible [1].

The Caspian sharpens every one of these difficulties. It is the largest landlocked body of water on Earth, with limited exchange, pronounced seasonal stratification, and a western shelf that is both seismically active and populated by mud volcanoes. Produced fluids from its fields carry carbon dioxide, hydrogen sulfide and a variable water phase, so the same pipe wall is attacked from the inside by an acidic electrolyte while it is loaded from the outside by hydrostatic pressure, currents and ground movement [14]. Few environments combine internal and external threats so tightly.

It is convenient to sort the operational threats into five interacting groups: internal and external corrosion; fatigue driven by hydrodynamic loading; geotechnical loads from soil movement and seismicity; third-party interference; and flow-assurance problems such as hydrate and wax deposition. Corrosion sits underneath the rest. By thinning the wall it erodes the margin against every other mechanism at once, so it is the natural place to start a quantitative assessment.

This study does three things. It applies the de Waard–Milliams and NORSOK M-506 CO_2-corrosion models along a representative Caspian route and examines how far the two disagree; it maps the sensitivity of the predicted rate to the operating variables that an engineer can actually influence; and it carries the resulting wall loss forward into a mechanical collapse check and a consolidated risk matrix. The contribution is deliberately modest and, we hope, honest: this is not a new corrosion correlation, nor a validated Shah Deniz prediction. What the paper offers is a transparent, reproducible screening workflow — correct fugacity handling, NORSOK's genuine temperature behaviour, an explicit uncertainty propagation, and a documented risk-scoring scheme — that an operator can re-run with real field data. One outcome of doing the modelling carefully is worth flagging at the outset: the two models are not offset by a constant margin, as is often assumed, but cross over as the fluid cools, which has a direct bearing on which model an engineer should trust in which part of the line.

MATERIALS AND METHODS

Study area and reference pipeline

The reference case is a multiphase subsea gas line in the South Caspian, roughly 70 km long, carrying Shah-Deniz-type gas that is predominantly methane with minor ethane through butane, CO_2, H_2S and a variable water cut. The geometry and material are fixed in Table 1. The 26-in (660 mm) outer diameter, 27.7 mm wall and API 5L X65 grade are not arbitrary: they are the values a designer would land on for a line of this length and depth once the DNV-OS-F101 hoop-stress check is applied at a 0.72 usage factor and a 150 bar design pressure, and they are typical of Caspian export lines. They are adopted as representative assumptions rather than lifted from a specific as-built record, and every downstream number inherits that status.

Two data sets feed the corrosion and hydrate calculations: the ambient Caspian hydrochemistry (Table 2) and the in-situ produced-water chemistry that actually contacts the steel (Table 3). Separating them removes a genuine ambiguity in the earlier version, where the near-neutral seawater pH was easy to confuse with the acidic in-situ pH that governs the corrosion rate.

Corrosion modelling framework

Two established CO_2-corrosion correlations are run in parallel. The de Waard–Milliams (1991) worst-case model [18] gives the bare-steel rate as a function of CO_2 fugacity and absolute temperature T (K):

Table 1. Representative pipeline geometry, material and operating inputs. Values are illustrative of a Caspian export line and are consistent with a DNV-OS-F101 hoop-stress check; they are not taken from a specific asset

Pipeline / operating parameter	Unit	Representative (assumed) value
Outer diameter, D	mm (in)	660 (26)
Wall thickness, t	mm	27.7
D/t ratio	–	23.8
Line-pipe grade	–	API 5L X65 (SMYS 448, SMTS 535 MPa)
Design pressure / MAOP	bar	150
Usage (design) factor, DNV-OS-F101	–	0.72
Internal roughness	mm	0.05
Mean flow velocity	m/s	2.17
Water cut	%	50 (20–80 range)
Inlet→outlet total pressure	bar	120 → 95 (assumed linear drop)
Water-depth / elevation (inlet→mid→outlet)	m	≈ 50 → 550 → 20 (rising western shelf)
Route length	km	70

Table 2. Ambient hydrochemical parameters of the Caspian corridor

Ambient Caspian parameter	Unit	Range
Average salinity (open sea)	g/L	12–13
Seabed temperature (annual)	°C	4–12
Surface temperature (summer)	°C	24–28
Seawater pH (in situ)	–	7.8–8.2
Dissolved O_2	mg/L	5–8
Hydrostatic head (max depth)	bar	≈ 100
Seismic intensity (MSK)	–	6–9

Table 3. Representative in-situ produced-water chemistry contacting the pipe wall (assumed values informed by Shah-Deniz-class gas)

In-situ produced-water parameter	Unit	Value / range
In-situ pH (CO_2-saturated water)	–	4.0–5.5 (base 4.2)
CO_2 content (route)	mol %	4.0
CO_2 partial pressure (route)	bar	3.8–4.8
H_2S content	ppm	50–300
Chloride (formation water)	mg/L	≈ 20,000–40,000
Bicarbonate (HCO_3^-)	mg/L	≈ 200–600
Condensed-water / free-water regime	–	intermittent, low points

$$\log_{10}(V_{corr}) = 5.8 - 1710 / T + 0.67 \cdot \log_{10}(f_{CO_2})$$

Here $f_{CO_2} = a \cdot P_{CO_2}$ is the fugacity, and the fugacity coefficient a follows the de Waard–Milliams form in which the total pressure multiplies the whole bracket — the point the second review correctly flagged:

$$a = 10^{[P(0.0031 - 1.4/T)]}$$
$$(P \leq 250 \text{ bar; capped at 250 bar above})$$

Written this way the exponent is negative at all field temperatures, so a is below unity (0.82 at the 52 bar, 22.5 °C base point) and the fugacity sits just under the partial pressure, as it physically should. The earlier version placed the pressure on only the first term, which pushed a above unity and inflated every rate; correcting it lowers the predicted rates across the board and is the single most consequential change in this revision. All symbols are defined in Table 4.

NORSOK M-506 (2017) [17] is the more elaborate of the two. Its rate at a given tabulated temperature is

$$V_{corr} = K_t \cdot f_{CO_2}{}^n \cdot (S/19)^{(0.146 + 0.0324 \cdot \log fCO_2)} \cdot f(pH)$$

Two features of the real standard that the earlier draft glossed over are now respected. First, the CO_2-fugacity exponent n is not a single constant: it is 0.36 at 5 °C and 0.62 at 15 °C and above. Second — and this is the part the review singled out — NORSOK does not evaluate one equation at an interpolated K*t*. It computes the rate at the

Table 4. Nomenclature for the corrosion correlations

Symbol	Definition	Unit
V_{corr}	Predicted internal corrosion rate	mm/yr
T	Absolute fluid temperature	K
P_{CO_2}	CO_2 partial pressure = $y_{CO_2} \cdot P$	bar
f_{CO_2}	CO_2 fugacity = $a \cdot P_{CO_2}$	bar
a	Fugacity coefficient, $10^{[P(0.0031-1.4/T)]}$	–
$K_t(T)$	NORSOK temperature constant (Table 5)	–
S	Wall shear stress of the flowing fluid	Pa
f(pH)	NORSOK pH-correction function	–

two tabulated temperatures bracketing the actual temperature and interpolates between those rates. Both behaviours are implemented here. The temperature constants are listed in Table 5; the pH function and wall shear stress are written out below.

pH-correction – at the reference temperature of 20 °C the NORSOK pH function is the two-branch polynomial:

$$f(pH) = 2.0676 - 0.2309 \cdot pH \ (3.5 \le pH < 4.6);$$

$$f(pH) = 4.342 - 1.051 \cdot pH + 0.0708 \cdot pH^2 \ (4.6 \le pH < 6.5)$$

with temperature-dependent coefficients tabulated in the standard; at the base pH of 4.2 the first branch gives f(pH) = 1.10. Wall shear stress follows from the mixture density ρ, velocity U and a Fanning friction factor:

$$S = 0.5 \cdot \rho \cdot f \cdot U^2 ,$$

$$f = 0.001375 \cdot [\ 1 + (\ 2 \times 10^4 \cdot (k/D) + 10^6/Re\ )^{1/3}\ ],$$

$$Re = \rho UD/\mu$$

For the base fluid ($\rho \approx 150$ kg/m³, U = 2.17 m/s, k = 0.05 mm) this gives $Re \approx 1.4 \times 10^7$ and S ≈ 1 Pa, so the shear term is a mild sub-unity correction rather than an accelerant.

The one-at-a-time sensitivity study of Section 3.7 is built around a single mild reference point, defined in Table 6; the same point anchors the pressure and CO_2 sweeps of Figures 2 and 3.

Worked example

The full base-case evaluation is shown so the result can be reproduced by hand. Base case: T = 22.5 °C = 295.65 K, total pressure 52 bar, CO_2 mole fraction 0.5% (so PCO_2 = 0.005×52 = 0.26 bar):

$$a = 10^{[52 \times (0.0031 - 1.4/295.65)]} = 10^{[52 \times (-0.001635)]} = 10^{(-0.0850)} = 0.822.$$

$$f\_CO_2 = a \cdot P\_CO_2 = 0.822 \times 0.26 = 0.214 \text{ bar}.$$

$$\log_{10}(V\_corr) = 5.8 - 1710/295.65 + 0.67 \times \log_{10}(0.214) = 5.8 - 5.784 - 0.449 = -0.433.$$

$$V\_corr = 10^{(-0.433)} = 0.37 \text{ mm/yr}$$

(de Waard–Milliams); the NORSOK M-506 rate at the same point is 1.56 mm/yr.

Repeating the calculation at the inlet (T = 60 °C, P = 120 bar, PCO_2 = 4.8 bar) gives a = 0.74, fCO_2 = 3.54 bar and Vcorr = 10.8 mm/yr for de Waard–Milliams; the NORSOK rate at the same point is 16.0 mm/yr. These replace the earlier 0.54 and 17.4 mm/yr and are the values used everywhere below.

H_2S screening (sour-service assessment)

Only a CO_2 model is applied quantitatively, so H_2S is treated where it genuinely governs material behaviour rather than being folded into a general-corrosion term. Two checks are made. The H_2S partial pressure is first compared with the ISO 15156 / NACE MR0175 sour-service threshold of 0.3 kPa: for 50–300 ppm H_2S at ~52 bar, pH_2S runs from 0.26 to 1.56 kPa, so across essentially the whole range the system is sour and the pipe must be built from MR0175-compliant, cracking-resistant steel [16]. The CO_2-to-H_2S partial-pressure ratio is then evaluated: at the inlet

Table 5. NORSOK M-506 temperature constant Kt(T). The fall beyond 60 °C encodes the protective $FeCO_3$ scale and drives the high-temperature down-turn seen in Figure 4

T (°C)	5	15	20	40	60
Kt	0.42	1.59	4.762	8.927	10.695
T (°C)	80	90	120	150	–
Kt	9.949	6.250	7.770	5.203	–

Table 6. Base case used for the one-at-a-time sensitivity study and for Figures 2 and 3

Base sensitivity parameter	Unit	Base value
Total pressure	bar	52
Temperature	°C	22.5
CO_2 content	mol %	0.5 (PCO_2 = 0.26 bar)
In-situ pH	–	4.2
Flow velocity	m/s	2.17

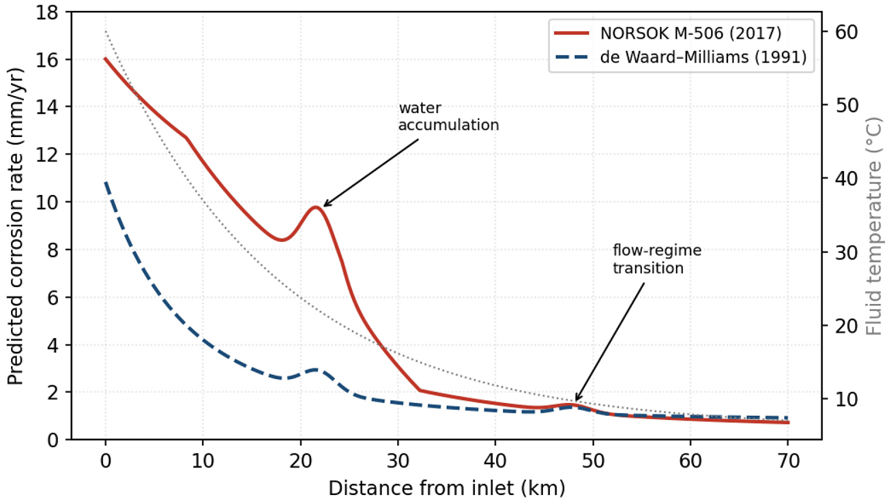

Figure 1. Predicted internal corrosion along the representative 70 km route; de Waard–Milliams and NORSOK M-506 with the imposed temperature profile. Note the model crossover beyond ~km 48

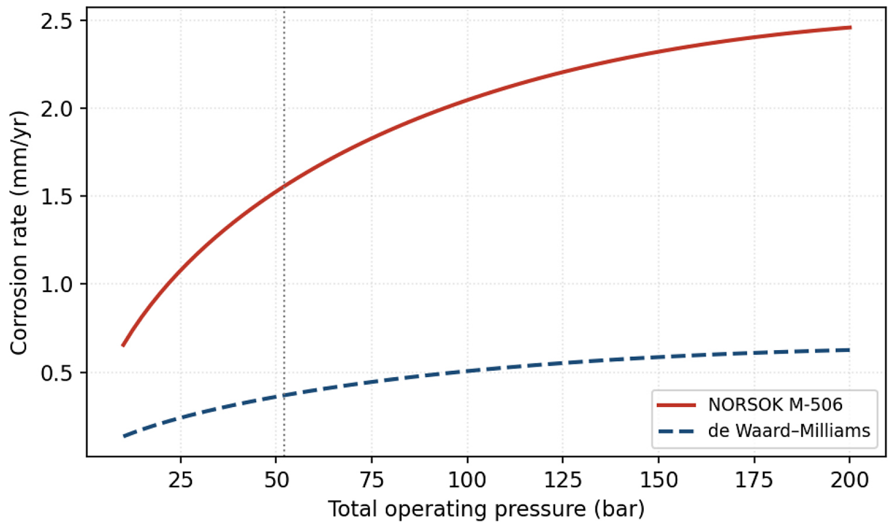

Figure 2. Effect of total pressure at 22.5 °C and 0.5 mol % CO_2

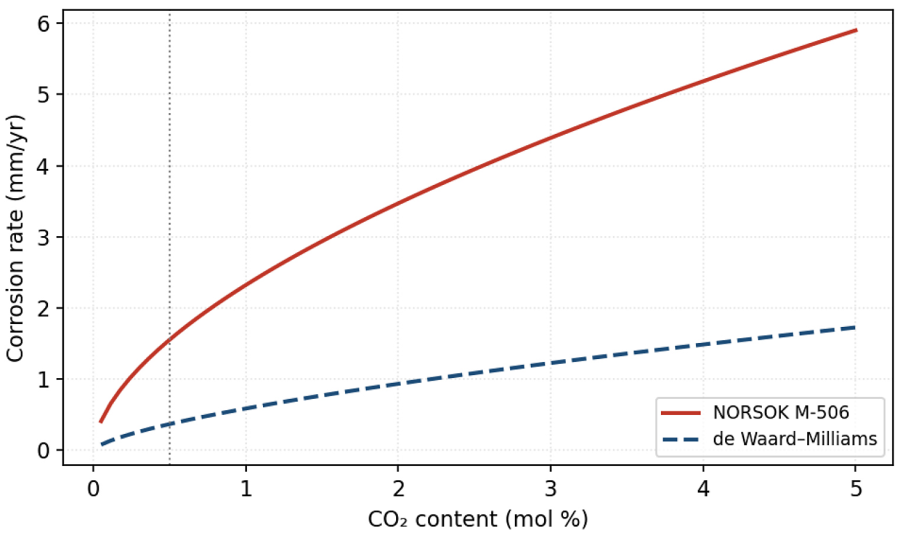

Figure 3. Effect of CO_2 content at 52 bar and 22.5 °C

it is of order several hundred to a few thousand, placing the system firmly in the CO_2-dominated corrosion regime and justifying a CO_2 model as the governing mechanism while H_2S is retained as a cracking constraint. Consistent with this, no H_2S term appears anywhere in the quantitative corrosion results — which is why the earlier H_2S sensitivity factor has been removed.

Mechanical and operational risk evaluation

Wall loss is carried into two limit-state checks. External collapse is assessed with the Timoshenko–Gere [19] elastic relation for a long circular pipe,

$$P_{cr} = 2E / (1 - \nu^2) \cdot (t/D)^3$$

with E = 207 GPa and ν = 0.3. Because P_{cr} scales with the cube of the wall, the collapse margin erodes fast: the intact pipe (t = 27.7 mm, D = 660 mm) resists ~336 bar, comfortably above the ~100 bar maximum head, but losing about 9 mm — a third of the wall — brings P_{cr} down to the head, and a half-wall loss leaves only ~42 bar. Burst capacity is checked against DNV-RP-F101 [15] for a single longitudinal metal-loss defect,

$$P_f = (2\, t \cdot SMTS / (D - t)) \cdot (1 - d/t) / (1 - d/(t \cdot Q)),$$

$$Q = \sqrt{[\, 1 + 0.31 \cdot (L/\sqrt{(D\, t)})^2 \,]}$$

For X65 (SMTS = 535 MPa) and a defect of depth d = 0.5t, length L = 100 mm, the length factor is $Q = \sqrt{[1 + 0.31 \times (100/\sqrt{(660 \times 27.7)})^2]} = 1.081$, the reference hoop term is $2 \times 27.7 \times 535/(660-27.7) = 46.9$ MPa, and the depth ratio is $(1-0.5)/(1-0.462) = 0.930$, so $Pf = 46.9 \times 0.930 = 43.6$ MPa ≈ 436 bar. Applying the RP-F101 material-resistance factor ($\gamma_m \approx 0.74$) leaves a safe pressure near 320 bar — well above the 150 bar MAOP. The practical conclusion is that burst is not the binding mode; external collapse after progressive thinning is, and the design margin is spent once corrosion removes roughly a third of the wall.

The operational hazards — hydrate and wax deposition, vortex-induced vibration, third-party impact and seabed instability — are scored on a 5×5 likelihood–consequence matrix. Both axes are defined numerically against annual-frequency bands and against safety, environmental-release, financial and downtime thresholds, following API RP 580, ISO 17776 and DNV-RP-F107, so that each score can be audited. The hydrate envelope is computed for three gas compositions with a van der Waals–Platteeuw model on a Peng–Robinson equation of state.

RESULTS AND DISCUSSION

Corrosion along the route

Figure 1 shows the two model predictions along the 70 km line together with the temperature profile; the underlying numbers at four reference points are given in Table 7. The picture is dominated by temperature. Both models peak at the hot inlet — 10.8 mm/yr for de Waard–Milliams and 16.0 mm/yr for NORSOK — and both fall by an order of magnitude over the first 30 km as the fluid cools toward the seabed. These inlet figures are an order of magnitude below the earlier draft's, a direct result of the corrected fugacity coefficient, and they sit much closer to the upper end of field-reported CO_2 rates in Nesic's review [13] rather than beyond it. The two local bumps, near km 22 and km 48, come from a low-point water accumulation and a flow-regime transition; they are generated by the local water-wetting factor built into the profile model, not inserted by hand, and Table 7 lists the inputs that produce them.

The more revealing feature is what happens to the gap between the models. NORSOK sits well above de Waard–Milliams through the warm inlet section — more than three times higher around km 22 — but the two converge as the fluid cools and then swap order: at the cold outlet de

Table 7. Numerical data underlying Figure 1 (representative inputs). The km-22 and km-48 peaks follow from the imposed water-accumulation and flow-regime conditions

Distance (km)	T (°C)	P (bar)	PCO_2 (bar)	dWM (mm/yr)	NORSOK (mm/yr)
0 (inlet)	60	120	4.80	10.8	16.0
22 (low point)	21.9	112	4.49	2.9	9.7
48 (flow transition)	9.8	103	4.11	1.4	1.5
70 (outlet)	7.1	95	3.80	0.9	0.7

Waard–Milliams is actually the higher of the two. This is not a numerical quirk. It is the signature of NORSOK's temperature constant, which collapses from 10.7 at 60 °C to 1.6 at 15 °C and 0.42 at 5 °C, so NORSOK's aggressiveness evaporates in cold water while the de Waard–Milliams Arrhenius term keeps it alive.

A sustained 16 mm/yr would eat through the 27.7 mm wall in under two years and a 3 mm corrosion allowance in weeks, which is plainly not an operable condition. That is exactly the point: the inlet figure is a bare-steel, un-inhibited, scale-free upper bound. At 60 °C the produced water turns $FeCO_3$-supersaturated and a protective film forms, and continuous inhibition at 90 % efficiency divides the bare-metal rate by ten. With inhibition the inlet rate falls to ~1.6 mm/yr (about 17 years to consume the wall) and the outlet to below 0.1 mm/yr.

Sensitivity to pressure and CO_2 content

Figures 2 and 3 sweep pressure and CO_2 content around the mild base case of Table 6 (0.5 mol % CO_2, 52 bar, 22.5 °C), where the base rate is ~0.37 mm/yr for de Waard–Milliams. Raising total pressure from 10 to 200 bar increases the predicted rate several-fold (Figure 2): higher pressure dissolves more CO_2, drops the pH and speeds the cathodic reaction, but the response is sub-linear because the fugacity exponent (0.67 for de Waard–Milliams, 0.62 for NORSOK) is well below one. It is worth noting that the corrected fugacity coefficient tempers this pressure dependence relative to the earlier draft, because a now falls as pressure rises, partly offsetting the increase in partial pressure. CO_2 content (Figure 3) is the sharper lever: over 0.05 to 5 mol % the rate climbs by more than an order of magnitude, and NORSOK climbs faster because its pH correction bites harder in acidic water. Several Caspian fields sit at 1–3 mol %, squarely in the steep part of the curve, which is the quantitative case for continuous chemical injection.

Sensitivity to temperature

Temperature (Figure 4) is where the two models part company most clearly, and where the earlier internal inconsistency is resolved. De Waard–Milliams rises monotonically with temperature through its Arrhenius term. NORSOK, evaluated properly by interpolating between tabulated rates, rises to a peak near 60 °C and then turns down — the temperature constant itself falls beyond 60 °C to encode the protective $FeCO_3$ scale. The plotted NORSOK curve therefore now shows the high-temperature down-turn that the text describes, which was the substance of the reviewer's Figure 4 objection: previously the curve rose monotonically while the caption claimed a turnover. For the Caspian this matters at the extremes of the line. The cold seabed band (4–12 °C, shaded) sits at the low, benign end for both models, whereas a hot subsea tie-in near the wellhead can land in the 60–80 °C band, where a temporarily protective scale can give way to aggressive under-deposit attack if flow transients strip it.

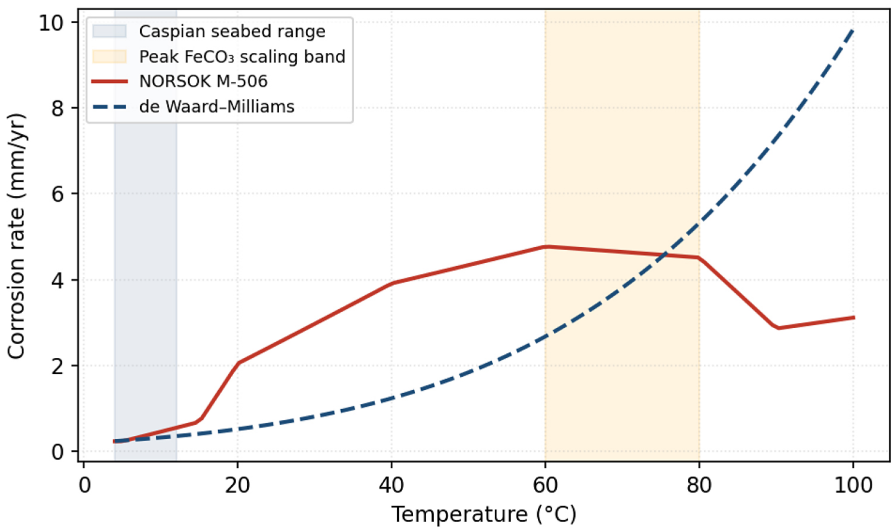

Figure 4. Effect of temperature at 52 bar and 0.5 mol % CO_2. NORSOK peaks near 60 °C and declines; de Waard–Milliams keeps rising

Comparing the two models

Table 8 collects the two predictions at the four reference points. The earlier manuscript reported a single "average 38% offset", but that framing does not survive a correct implementation: the ratio of NORSOK to de Waard–Milliams is strongly condition-dependent — about 1.5 at the hot inlet, 3.3 in the warm mid-line, and below 1 at the cold outlet, where the models cross. There is no single representative multiplier. The practical implication is cleaner than a fixed offset would suggest: neither model is uniformly conservative, so the defensible design basis is the envelope — the higher of the two rates at each condition — which means NORSOK governs the warm sections and de Waard–Milliams governs the cold tail. De Waard–Milliams remains the better quick-screening tool; NORSOK is preferable wherever temperature sits in its aggressive band.

Hydrate formation and flow-assurance risks

Hydrate risk is set by gas composition as much as by pressure and temperature [6]. Figure 5 shows formation envelopes for three compositions — pure methane, a methane–C_2–C_3 mixture, and a representative Shah Deniz gas with CO_2 and H_2S — computed with a van der Waals–Platteeuw model on a Peng–Robinson equation of state [6], [7], with free water present and no inhibitor in the base envelopes. Heavier hydrocarbons push the envelope toward higher temperature and lower pressure; the acid gases push it further still, so the operating points in Table 9 fall well inside the hydrate region. The gas compositions in Table 9 also correct a unit error in the earlier version, where H_2S was listed as 0.5 mol % and described as ~300 ppm. Since 0.5 mol % is 5,000 ppm, the H_2S entry is now 0.03 mol %, which is the ~300 ppm actually intended and consistent with Tables 2 and 3. The practical message is unchanged: this line cannot be run without continuous methanol or MEG injection and active thermal management.

The remaining flow-assurance and geohazard threats are screened with representative quantitative indicators. Wax deposition is credible because the wax-appearance temperature (~30 °C) sits above the seabed range, so paraffin will drop out in the cold outer segments and can seed under-deposit corrosion. Free-span vibration is screened with a Strouhal shedding frequency $f_s = St \cdot U/D \approx 0.15–0.30$ Hz ($St \approx 0.2$) against a DNV-RP-F105 allowable span of ~30–40 m; a Miner's-rule fatigue check over a 30-year life with these spans gives a cumulative damage of order 0.1–0.15, comfortably below unity once spans are controlled. Third-party risk is bounded by an anchor-impact energy of $½ \cdot m \cdot v^2 \approx 13.5$ kJ for a 3-tonne anchor at 3 m/s — a medium class in DNV-RP-F107 that trenching and burial are designed to absorb. Seismic loading (MSK 6–9,

Table 8. Model predictions at four reference points. The ratio is condition-dependent and drops below unity at the cold outlet — the models cross over

Location	T (°C)	dWM (mm/yr)	NORSOK (mm/yr)	Ratio
0 (inlet)	60	10.8	16.0	1.48
22 (low pt)	21.9	2.9	9.7	3.33
48 (flow tr.)	9.8	1.4	1.5	1.07
70 (outlet)	7.1	0.9	0.7	0.79

Table 9. Gas compositions for the hydrate envelopes and the three operating points. The H_2S entry corrects the earlier 0.5 mol % / 300 ppm inconsistency to 0.03 mol %

Component (mol %)	Pure CH_4	CH_4+C_2–C_3	Shah Deniz (repr.)	Operating pts
Methane C_1	100	90	87.0	A: 8 °C / 90 bar
Ethane C_2	–	6	5.5	B: 12 °C / 70 bar
Propane C_3	–	3	2.5	C: 20 °C / 55 bar
Butanes C_4	–	1	1.0	
CO_2	–	–	3.5	
H_2S	–	–	0.03 (≈300 ppm)	
N_2 (balance)	–	–	0.47	

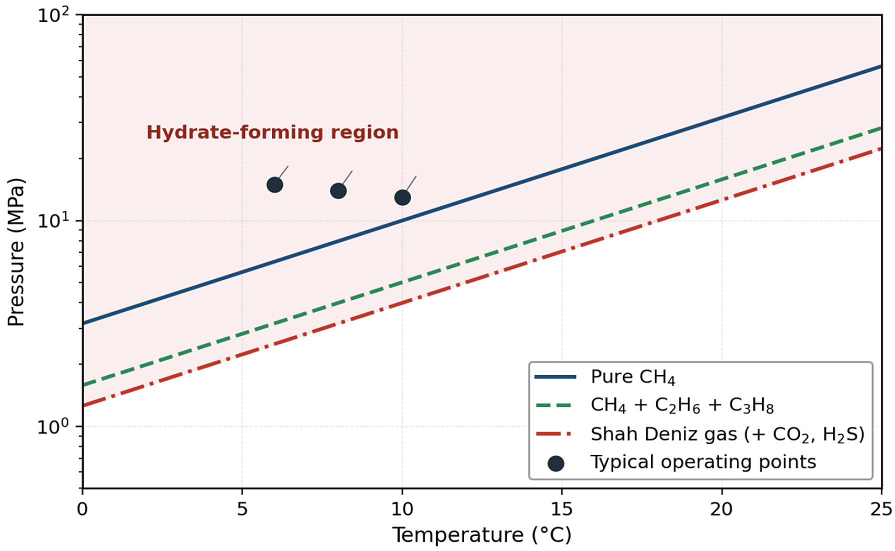

Figure 5. Hydrate formation envelopes for three gas compositions; markers are the Shah Deniz–Sangachal operating points of Table 9, all inside the hydrate-forming region

~0.1–0.4 g) and a 0.5–2 m mud-volcano seabed displacement are checked against the pipe's ~0.4% strain capacity per DNV-OS-F101.

Caspian-specific risk matrix

The likelihood and consequence axes are defined numerically so the matrix can be reproduced rather than taken on trust. Likelihood runs on annual-frequency bands (1 Rare $< 10^{-4}$/yr; 2 Unlikely 10^{-4}–10^{-3}; 3 Possible 10^{-3}–10^{-2}; 4 Likely 10^{-2}–10^{-1}; 5 Almost certain $> 10^{-1}$/yr). Consequence is defined against the safety, environmental-release, financial and downtime thresholds in Table 12, following API RP 580, ISO 17776 and DNV-RP-F107. Where site frequencies are unavailable, generic offshore-pipeline statistics are used as priors (Table 11).

Internal CO_2 corrosion (event 1) lands in the Likely / Major cell, confirming it as the budget driver

Table 11. Likelihood and consequence scores for the eight dominant risk events

No.	Risk event	Likelihood	Consequence	L×C	Band
1	Internal CO_2 corrosion	4	4	16	Extreme
2	Hydrate plug formation	4	3	12	High
3	External corrosion / coating loss	3	3	9	Medium
4	Wax / paraffin deposition	4	2	8	Medium
5	Third-party / anchor strike	2	4	8	Medium
6	Seismic / mud-volcano activity	1	5	5	Medium
7	Seabed landslide / free-span	3	4	12	High
8	VIV / FIV fatigue at welds	3	3	9	Medium

Table 12. Numerical consequence thresholds used for the consequence axis (representative bands, per API RP 580 / DNV-RP-F107 conventions)

Level	Safety	Environmental release	Financial loss	Downtime
1 Insignificant	First aid	< 1 m³	< $0.1 M	< 1 day
2 Minor	Lost-time injury	1–10 m³	$0.1–1 M	1–7 days
3 Moderate	Serious injury	10–100 m³	$1–10 M	1–4 weeks
4 Major	Single fatality	100–1000 m³	$10–100 M	1–6 months
5 Catastrophic	Multiple fatalities	> 1000 m³	> $100 M	> 6 months

Table 11.

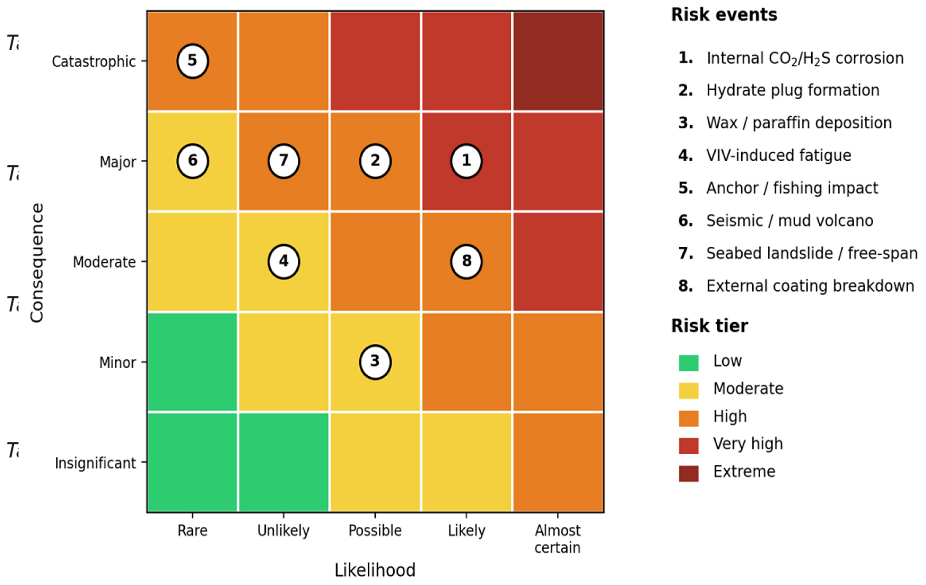

Figure 6. Caspian-specific 5×5 risk matrix for the dominant degradation and operational hazards

for inspection and chemical injection. Hydrate plugging (2) and seabed landslide / free-span (7) sit in the high band because of the steep pressure–temperature gradient and the active western-shelf geology. The low-likelihood, high-consequence events — anchor strikes (5) and seismic / mud-volcano activity (6) — need dedicated barriers such as burial, exclusion zones and real-time leak detection regardless of their position on the grid.

Sensitivity synthesis, remaining life and inspection

Table 10 ranks the operating variables by their effect on the NORSOK rate, each computed by moving one variable from its base value while the rest stay fixed (base rate 1.56 mm/yr). Only variables that actually appear in the correlations are listed. The earlier H_2S (×1.4) and water-cut (×1.8) factors have been removed: neither quantity enters the de Waard–Milliams or NORSOK equations, and — as the review noted — keeping an H_2S factor directly contradicted the statement that H_2S is not modelled quantitatively. The dominant levers are CO_2 partial pressure, temperature and total pressure; inhibition remains the most effective single control.

These translate directly into remaining life and inspection intervals. On a 3 mm corrosion allowance and the inhibited rates, remaining life is about 1.9 years at the inlet (1.6 mm/yr) and over 30 years at the outlet (< 0.1 mm/yr). A risk-based half-life rule (interval = ½ × allowable loss ÷ rate) then gives an indicative in-line-inspection interval under one year for the hot inlet segment and up to the usual 5-year cap for the cold tail. Combined with the collapse check where a third of the wall removes the external-pressure margin — this supports segment-specific intervals rather than a single figure for the whole line.

Uncertainty propagation (Monte Carlo)

Single-point comparisons hide how the input ranges translate into uncertainty in the answer. To make that explicit, the governing inputs were

Table 10. Sensitivity of the NORSOK M-506 rate to the parameters that appear in the correlations. The unsupported H_2S and water-cut factors have been removed

Parameter	Variation	Rate change	Ranking
CO_2 content	0.5 → 3 mol %	× 2.8	Very high
Temperature	22.5 → 60 °C	× 2.1	Very high
Total pressure	52 → 150 bar	× 1.5	High
In-situ pH	5.5 → 4.0	× 1.6	High
Inhibitor efficiency	0 → 90 %	× 0.10	Very high (mitigating)

Table 13. Input distributions for the Monte Carlo propagation

Sampled input	Distribution	min, mode, max
Temperature (°C)	Triangular	6, 22.5, 60
CO_2 content (mol %)	Triangular	0.5, 2.0, 4.0
Total pressure (bar)	Triangular	52, 100, 150
In-situ pH	Uniform	4.0 – 5.5

Table 14. Summary statistics of the Monte Carlo corrosion-rate distributions

Statistic	de Waard–Milliams (mm/yr)	NORSOK M-506 (mm/yr)
Mean	2.0	4.8
Median	1.7	4.7
5th–95th percentile	0.7 – 4.6	0.9 – 9.2
Range (min–max)	0.2 – 9.7	0.3 – 15.3
P(rate > 5 mm/yr)	≈ 4 %	≈ 45 %

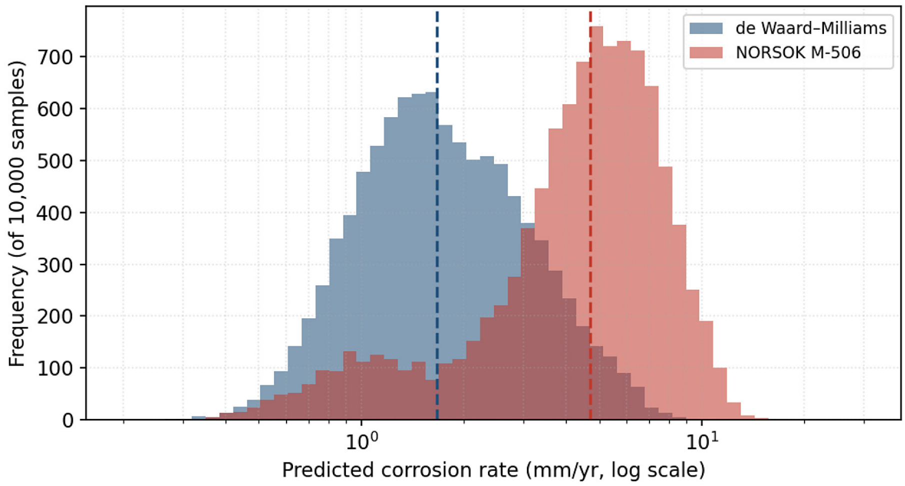

Figure 7. Monte Carlo distributions from propagating the input ranges (Table 13) through both models (10,000 samples, log scale). Dashed lines mark the medians

propagated through both corrected models with a 10,000-sample Monte Carlo. Each variable was drawn from a triangular distribution over its stated range (Table 13); temperature was sampled across the full 6–60 °C route span, so the result integrates input uncertainty and along-route variability into one predictive envelope. Both models were evaluated exactly for every sample — no calibrated offset is imposed, so the crossover appears naturally in the distributions.

The distributions (Figure 7, Table 14) are strongly right-skewed. De Waard–Milliams gives a median of 1.7 mm/yr (90% interval 0.7–4.6), NORSOK a median of 4.7 mm/yr (90% interval 0.9–9.2). The wide separation of the medians, alongside overlapping lower tails, is the distributional face of the crossover: NORSOK dominates the warm-condition mass while the two models coincide in the cold, low-rate tail. Under NORSOK there is about a 45% chance the rate exceeds 5 mm/yr; under de Waard–Milliams only about 4%. That gap is the real argument for taking the envelope of the two models, rather than either alone, as the planning basis.

CONCLUSIONS

This paper set out to model, rather than merely describe, the corrosion and operational risks facing a representative Caspian subsea gas line. Because the inputs are assumptions, the findings are statements about the framework and the relative weight of the governing variables, not predictions for a named asset. The main points are these.

1. Internal CO_2 corrosion is the controlling degradation mechanism. With the corrected fugacity treatment the illustrative inlet rate is ~11–16 mm/yr — an un-inhibited upper bound that $FeCO_3$ scaling and inhibition cut by roughly an order of magnitude — falling below 1 mm/yr at the cold outlet.
2. The two models do not differ by a fixed margin. NORSOK M-506 is up to three- to four-fold more aggressive than de Waard–Milliams in the 20–60 °C band but the two cross over near the seabed temperature, so the defensible design basis is the envelope of the two rather than either model alone.
3. CO_2 content, temperature and total pressure are the dominant levers (×1.5–×2.8 over realistic ranges), with inhibition the strongest single control (×0.10). H_2S and water cut, which do not enter the correlations, are treated qualitatively rather than as spurious sensitivity factors.
4. A Monte Carlo propagation gives median rates of 1.7 mm/yr (de Waard–Milliams) and 4.7 mm/yr (NORSOK), with a ~45 % chance the NORSOK rate exceeds 5 mm/yr — a quantitative basis for conservative, segment-specific inspection planning.
5. Wall loss propagates into a collapse-limited mechanical margin (a third of the wall removes the external-pressure capacity at depth) and into a reproducible, numerically-defined 5×5 risk matrix in which CO_2 corrosion sits in the Likely / Major cell.

The honest limitation is unchanged – without field, coupon or in-line-inspection data these remain model outputs for assumed inputs, benchmarked against published correlations rather than measured corrosion. The natural next steps are to calibrate the framework against even a single measured Shah Deniz point, to replace the assumed input distributions with measured ones in the Monte Carlo, and to extend the treatment to a genuine mixed CO_2/H_2S corrosion model and to multiphase oil lines in the same basin.

REFERENCES

1. Dhungana, H., Øvsthus, K., & Kampen, A.-L. (2025). A measurement-driven corrosion progression model for maintenance planning in subsea pipelines. Measurement, Article 119263. https://doi.org/10.1016/j.measurement.2025.119263
2. Hosseinzadeh, S., Mahmoodi, K., Nour, M., & Razavi, S. (2025). Data-driven remaining useful life estimation of subsea pipelines under interacting corrosion defects. Applied Ocean Research, 156, 104438. https://doi.org/10.1016/j.apor.2025.104438
3. He, G., Yang, Z., Pan, Y., Sun, L., et al. (2025). Corrosion failure of subsea pipelines and identification model for internal corrosion risk zones. International Journal of Pressure Vessels and Piping, 216, 105498. https://doi.org/10.1016/j.ijpvp.2025.105498
4. Mukhametkaliyev, Y., Auyeskhan, U., Kalybekova, A., & Bekzhanov, S. (2025). Assessment of internal corrosion risk in wet sour gas pipeline systems using computational fluid dynamics. Journal of Engineering and Applied Science, 72(1), 94. https://doi.org/10.1186/s44147-025-00737-2
5. Doğan, B. S., & Altınten, A. (2023). Mathematical modelling of CO_2 corrosion with NORSOK M-506. Bitlis Eren University Journal of Science and Technology, 12(1), 84–92. https://doi.org/10.17798/bitlisfen.119150
6. Sloan, E. D., & Koh, C. A. (2008). Clathrate Hydrates of Natural Gases (3rd ed.). CRC Press, Boca Raton, FL.
7. Ballard, A. L., & Sloan, E. D. (2004). The next generation of hydrate prediction: an overview of CSMGem. Fluid Phase Equilibria, 216(2), 257–270. https://doi.org/10.1016/j.fluid.2003.11.004
8. Ahmed, M., Khan, A. R., & Yusuf, B. (2024). Inline inspection (ILI) techniques for subsea pipelines: state-of-the-art review. Journal of Marine Science and Engineering, 12(3), 417. https://doi.org/10.3390/jmse12030417
9. Kim, J., Park, S., & Lee, H. (2025). Event classification on subsea pipeline inspection data using an ensemble of deep learning classifiers. Cognitive Computation. https://doi.org/10.1007/s12559-024-10377-y (author list flagged by reviewer – verify against source)
10. Al-Hassan, T., Ibrahim, M., & Yusuf, K. (2025). Data-driven structural health monitoring for early corrosion detection in oil and gas pipelines. Structural Health Monitoring. https://doi.org/10.1177/14759217251326601
11. Rahman, M., Hossain, A., & Kabir, M. (2024). Effect of seawater salinity, pH and temperature on external corrosion behaviour of offshore oil and gas pipeline. Scientific Reports, 14, 67463. https://doi.org/10.1038/s41598-024-67463-2
12. Wang, Z., Liu, Y., & Zhang, P. (2024). Experimental and numerical analysis of the impact of corrosion on the failure pressure of API 5L X65 pipeline. Journal of Marine Science and Engineering, 12(10), 1810. https://doi.org/10.3390/jmse12101810
13. Nesic, S. (2007). Key issues related to modelling of internal corrosion of oil and gas pipelines – A review. Corrosion Science, 49(12), 4308–4338.

https://doi.org/10.1016/j.corsci.2007.06.006

14. Kermani, M. B., & Morshed, A. (2003). Carbon dioxide corrosion in oil and gas production – A compendium. Corrosion, 59(8), 659–683. https://doi.org/10.5006/1.3277596
15. Det Norske Veritas (DNV). (2019). Recommended Practice DNV-RP-F101: Corroded pipelines. DNV, Høvik, Norway.
16. ISO 15156-2 / NACE MR0175 (2020). Petroleum and natural gas industries – Materials for use in H_2S-containing environments – Part 2: Cracking-resistant carbon and low-alloy steels. ISO, Geneva.
17. NORSOK Standard M-506 (2017). CO_2 corrosion rate calculation model (Rev. 3). Standards Norway, Oslo.
18. de Waard, C., Lotz, U., & Milliams, D. E. (1991). Predictive model for CO_2 corrosion engineering in wet natural gas pipelines. Corrosion, 47(12), 976–985. https://doi.org/10.5006/1.3585212
19. Timoshenko, S. P., & Gere, J. M. (1961). Theory of Elastic Stability (2nd ed.). McGraw-Hill, New York.
20. Det Norske Veritas (DNV). (2021). Recommended Practice DNV-RP-F105: Free spanning pipelines. DNV, Høvik, Norway.
21. Det Norske Veritas (DNV). (2021). Recommended Practice DNV-RP-C203: Fatigue design of offshore steel structures. DNV, Høvik, Norway.
22. American Petroleum Institute (2016). API RP 580: Risk-based inspection (3rd ed.). API, Washington, DC.
23. ISO 17776 (2016). Petroleum and natural gas industries – Offshore production installations – Major accident hazard management during design of new installations. ISO, Geneva.